

UC Santa Barbara

UC Santa Barbara Previously Published Works

Title

Hot carrier filtering in solution processed heterostructures: a paradigm for improving thermoelectric efficiency.

Permalink

<https://escholarship.org/uc/item/6nv7n9fp>

Journal

Advanced materials (Deerfield Beach, Fla.), 26(17)

ISSN

0935-9648

Authors

Zhang, Yichi
Bahk, Je-Hyeong
Lee, Joun
[et al.](#)

Publication Date

2014-05-01

DOI

10.1002/adma.201304419

Copyright Information

This work is made available under the terms of a Creative Commons Attribution-NonCommercial-NoDerivatives License, available at <https://creativecommons.org/licenses/by-nc-nd/4.0/>

Peer reviewed

Hot Carrier Filtering in Solution Processed Hetero-structures: a Paradigm for Improving Thermoelectric Efficiency

By Yichi Zhang, Je-Hyeong Bahk, Joun Lee, Christina S. Birkel, Matthew L. Snedaker, Deyu Liu, Hongmei Zeng, Martin Moskovits, Ali Shakouri, and Galen D. Stucky*

[*] Prof. Galen D. Stucky, Dr. Yichi Zhang, Dr. Joun Lee, Dr. Christina S. Birkel, Mr. Matthew L. Snedaker, Mr. Deyu Liu, Dr. Hongmei Zeng, Prof. Martin Moskovits
Department of Chemistry and Biochemistry, University of California-Santa Barbara,
Santa Barbara, CA 93106, (U.S.)
E-mail: (stucky@chem.ucsb.edu)

Dr. Je-Hyeong Bahk, Prof. Ali Shakouri
Birck Nanotechnology Center, Purdue University,
West Lafayette, IN 47907, (U.S.)

Dr. Christina S. Birkel
Materials Research Laboratory, University of California-Santa Barbara,
Santa Barbara, CA 93106-5121, (U.S.)

Prof. Ali Shakouri
Department of Electrical Engineering, University of California-Santa Cruz,
Santa Cruz, CA 95064, (U.S.)

Prof. Galen D. Stucky
Materials Department, University of California-Santa Barbara
Santa Barbara, California, 93106, (U.S.)

Keywords: thermoelectric, hot carrier filtering effect, solution processed, hetero-structure, molecular metal chalcogenide, atomic layer deposition (ALD)

The large-scale use of thermoelectrics for conversion of waste heat to electricity is currently limited by materials cost and efficiency. The efficiency of a thermoelectric (TE) is normally expressed through its figure of merit $zT = S^2\sigma T/\kappa$, where S is the Seebeck coefficient, σ is the electrical conductivity, κ is the thermal conductivity, and T is the absolute temperature. A strategy that could lead to an efficient and economical thermoelectric is to fabricate nanostructured materials incorporating nanograins^[1-4] or pores,^[5,6] thereby reducing the material's thermal conductivity by disrupting the crystal's phonon transport and consequently the lattice contribution to its thermal conductivity.^[7] This strategy has been shown to be effective in single-phase systems, such as p-type (Bi, Sb)₂Te₃, half-Heusler and Si_xGe_{1-x}, produced by high-energy ball milling.^[2-4] Notably, a hierarchical PbTe material with a bulk record $zT \approx 2.2$ has been reported.^[8] However, ball milling is not scalable cost-effectively. More to the point, little room remains for further reducing κ by nanostructuring single-phase materials because the electronic contribution to κ cannot be decoupled from σ (Wiedemann-

Franz law), while the lattice contribution cannot be reduced below the amorphous limit, which has essentially been reached, particularly for the Bi₂Te₃ system whose reported lattice contribution has approached to the lower limit ($\sim 0.3 \text{ W m}^{-1} \text{ K}^{-1}$ *a-b* axis at 300 K) as predicted by the Cahill model.^[3,9] Further improvements in the figure of merit must rely on new paradigms for nanostructuring multi-phase materials through which the interdependence of *S* and σ is decoupled, or better still, synergistically modified.

This article describes such a new approach based on a scalable, low-cost, solution-based synthesis that produces a stable Ag/oxide/Sb₂Te₃-Te metal-semiconductor hetero-structure that achieves a figure of merit $zT = 1.0$ at 460 K, a record for a hetero-structured material made by using wet chemistry. Moreover, by complementing our experimental data with theory, we show unequivocally that the large increase in the material's Seebeck coefficient results from hot carrier filtering: a process that had been proposed by theory but never previously observed in poly-crystal films.

Two approaches have been demonstrated to increase *S*, thereby simultaneously enhancing of *S* and $S^2\sigma$: (a) increasing the local density of states (DOS) at the Fermi level, and (b) filtering out cold carriers *via* band offset, which, respectively, modify the energy derivative of the number of carriers, $dn(E)/dE$, and of the carrier mobility, $d\mu(E)/dE$, terms in the Mott expression (Equation (1)).

$$S = \frac{\pi^2 k_B^2 T}{3q} \left\{ \frac{d[\ln(\sigma(E))]}{dE} \right\}_{E=E_F} = \frac{\pi^2 k_B^2 T}{3q} \left\{ \frac{dn(E)}{n dE} + \frac{d\mu(E)}{\mu dE} \right\}_{E=E_F} \quad (1)$$

(k_B is the Boltzmann constant, and q is electron charge.) Modification of the former term was demonstrated experimentally by Heremans and co-workers in Tl-doped PbTe with a distortion of the electronic DOS.^[10] In contrast, improvement based on the latter mechanism, the hot carrier filtering effect, might be obtained by synthetic structural and electronic integration of multiple phases. In this way, the interfacial potential between phases will selectively filter out the carriers with low energy thereby increasing $d\mu(E)/dE$. In attempts to achieve this, a variety of phase combinations such as metal-semiconductor and semiconductor-semiconductor have been investigated.^[11-17] For example, the band bending between metals and semiconductors was shown to provide the interfacial potential necessary to selectively scatter low-energy carriers,^[11,12,15] while a similar interfacial band offset in the semiconducting superlattice InGaAs/InGaAlAs and PbTe/PbSe core-shell structures plays the same role as a hot carrier filtering barrier.^[13,17]

In those experimental reports, phase-segregation from solid solutions was widely used to produce hetero-structured bulk materials. However, this top-down strategy is limited by the controllable preparation of several phase combinations defined by both the appropriate dimensions and compositions. Alternatively, a bottom-up approach is more versatile in making it possible to build up targeted phases using molecular/nanoscaled building blocks, thereby greatly expanding the library of phase combinations. Among the bottom-up strategies, a solution process is desirable for its low cost and easy scale-up of the synthesis and for its application to a large variety of material systems. However, most of the reported solution approaches have been aimed at single-phased material rather than hetero-structures, and the

zT values achieved were significantly lower than those resulting from thermoelectric materials made by state-of-the-art ball milling.^[18,19] For example, for p-type bismuth telluride, the highest zT reported by solution processing using hydrazine soluble molecular metal chalcogenide (MMC) chemistry^[20] is 0.6,^[19] ~50% lower than the reported record for the same composition made using ball milling.^[3]

Here we report a novel hetero-structured Ag/oxide/Sb₂Te₃-Te, with $zT \sim 1.0$ at 460 K, significantly improving on previous solution-processed single-phased thermoelectric materials. More importantly, we were able to successfully stabilize a metallic silver phase in a telluride matrix by coating the silver in a thin oxide layer thereby producing a phase combination that does not form naturally because of the high solubility of silver in telluride under mild heating (~200 °C). Meanwhile, the oxide layer prevents silver atoms from alloying with telluride during annealing, thereby maintaining the carrier density in the optimal range ($5\text{-}8 \times 10^{19} / \text{cm}^3$). This mitigates the degradation of the Seebeck coefficient that we had previously observed.^[12] Theoretical modeling verifies that the high Seebeck coefficient and zT of this hetero-structure are successfully explained by a hot carrier filtering model with an interfacial band offset of 0.2-0.3 eV, close to the theoretically predicted optimal value.^[17,21,22] To the best of our knowledge, this is the first report of this effect for a bulk, poly-crystallized material system processed in solution with both experimental observations and theoretical simulations. In addition to the advantage of preparation cost, the hetero-structure exhibits both thermal stability and enhanced TE performance. We believe that these results will enable the optimal and novel design of thermally stabilized hetero-phases in other material systems to further improve TE material conversion performance.

The hetero-structured film that we will refer to as Ag/oxide/Sb₂Te₃-Te was fabricated as shown in **Figure 1 (a)**. Two-dimensional (2D) array of silver NPs were first prepared by e-beam evaporating an 8-nm (mass thickness) silver film (99.999%) on a quartz substrate then, using rapid thermal annealing, converting the silver film to a 2D array of NPs with a diameter of 40 ± 10 nm (s.d.). Two oxide layers: aluminum oxide (~1-2 nm) and hafnium oxide (~1 nm) were sequentially deposited using atomic layer deposition (ALD) on the exposed surface of the silver. In the final step, we used the hydrazine chemistry that has been developed previously.^[19,20] Specifically, a solution containing Sb₂Te₃ with excess Te was cast on the substrates to cover the silver particles, following an annealing process at 200 °C. Control samples, referred to as Ag/Sb₂Te₃-Te and Sb₂Te₃-Te, (e.g. in **Figure 2**), were synthesized by skipping step 2 (thin oxide coating); or, both step 1 (forming of silver NPs) and step 2, while retaining all other step(s).

Secondary ion mass spectroscopy (SIMS) (Figure 1 (b)) combined with cross-sectional SEM imaging (Figure 1 (c)) confirmed the layered structures of the film. Specifically, a depth profile comparison between Ag/oxide/Sb₂Te₃-Te film and a homogeneous film, AgSbTe₂, which was prepared by casting a similar precursor containing cubic AgSbTe₂ compound and Te, shows that the relative ¹⁰⁷Ag signal increases significantly on the bottom for Ag/oxide/Sb₂Te₃-Te. This confirms that the silver atoms primarily accumulated on the bottom of the film for the hetero-structure. It is worth noting that the distribution profiles shown in this figure are broadened by the roughness of the film. SEM (Figure 1(c)) further

confirms these morphologies and structural layers. The blue layer corresponds to the layer of solution-cast Sb_2Te_3 and Te. It contains sub-micron scale pores formed by ligand decomposition during annealing. The inset image highlights the hemi-spherical shaped thin oxide layer, and further confirms the existence of thin oxide coated silver NPs on the bottom of the film. X-ray diffraction (Figure 1(d)) confirmed the existence of two main phases, rhombohedral Sb_2Te_3 and hexagonal Te, in the three samples (Sb_2Te_3 -Te, Ag/oxide/ Sb_2Te_3 -Te, Ag/ Sb_2Te_3 -Te). The high doping level and inter-metallic impurities in the Ag/ Sb_2Te_3 -Te sample were not taken into account in the Rietveld refinement, which resulted in larger error than for the other samples in the fitting of the experimental X-ray diffraction patterns.

The composition and thickness of the oxide layer that covers the silver particles in Ag/oxide/ Sb_2Te_3 -Te are critical in defining the overall TE properties. Trimethylaluminum and vaporized water were chosen to grow amorphous Al_2O_3 with a thickness from 1 to 2 nm during ALD coatings. This avoids the silver oxidation that results if oxygen plasma is used. The main function of the Al_2O_3 layer is to protect the silver NPs and prevent the diffusion of silver. On the surface of Al_2O_3 , a second layer of oxide, HfO_2 (~ 1 nm) was deposited to prevent the etching of Al_2O_3 by the basic ($\text{pH} \approx 9$) hydrazine solutions that were used to cast the metal chalcogenide in the following step. The total thickness of the dielectric layer was minimized in order to facilitate carrier tunneling and maintain the high electrical conductivity. The optimum thickness of the oxide layer in terms of the TE performance was determined by investigating the electronic properties of several Ag/oxide/ Sb_2Te_3 -Te samples with different oxide thicknesses. As shown in Figure 2(a), the one with 1 nm Al_2O_3 and 1 nm HfO_2 , 2 nm in total, is more electrically conductive than the one with 2 nm Al_2O_3 and 1 nm HfO_2 , 3 nm in total. However, the Seebeck coefficient of the 2-nm sample is lower than that of the one with a 3-nm oxide layer since the thin oxide layer of 2 nm in total is not thick enough to form a pinhole-free layer that effectively limits the diffusion of silver atoms. With the 2-nm oxide coating, the silver atoms can still alloy with telluride acting as dopants, resulting in a dramatic increase in the overall number of carriers, which is not favored in terms of TE performance. This behavior is similar to that observed for Ag/ Sb_2Te_3 -Te, in which the silver particles do not have an oxide layer. A complementary comparison of the properties of Ag/oxide/ Sb_2Te_3 -Te with various total thicknesses of oxide is presented in the supporting information as **Table S1**. In summary, 2 nm Al_2O_3 plus 1 nm HfO_2 is the optimal thickness and composition for the purpose of protecting silver NPs. A thinner layer than the optimum does not provide the required chemical confinement for the silver NPs and enhancement of the Seebeck coefficient. A thicker layer than the optimum jeopardizes the transport of carriers from Ag to Sb_2Te_3 and Te, and thereby leads to the degradation of conductivity. Accordingly, in the discussion of this paper, Ag/oxide/ Sb_2Te_3 -Te refers to the sample with optimum thickness and composition (2 nm Al_2O_3 plus 1 nm HfO_2) unless otherwise specified.

In Figure 2(b)-(d), two control samples, Sb_2Te_3 -Te (black squares) and Ag/ Sb_2Te_3 -Te (orange triangles) are compared with Ag/oxide/ Sb_2Te_3 -Te (blue circles). The errors include the variation from batch to batch and the measurement error from cycle to cycle. Compared to the Seebeck-coefficient errors, the test errors in the measurement of electrical conductivity are negligible. In addition, no significant trend of variation can be observed from the first cycle to the last. The oxide-coated sample exhibits the highest power factor $S^2\sigma$ ($\sim 10 \mu\text{W}/(\text{cm}\cdot\text{K}^2)$) at

~300 K); this is the result of a significantly higher Seebeck coefficient than that of Ag/Sb₂Te₃ and a respectable electrical conductivity that is between those of Ag/Sb₂Te₃ and Sb₂Te₃-Te. The behaviors of these three samples can be well explained by the carrier densities at room temperature. Although the thin (3-nm) oxide layer in Ag/oxide/Sb₂Te₃-Te prevents most of the silver atoms from alloying with telluride, a small number of silver atoms still dope into the telluride to slightly increase the hole density from $\sim 3 \times 10^{19}$ to $\sim 6 \times 10^{19}$ /cm³ (inset table in Figure 3). According to the literature on silver doped Sb₂Te₃,^[23] one silver atom in Sb₂Te₃ acts as an acceptor to produce two holes, so that the doped concentration of a silver impurity in Sb₂Te₃-Te matrix of Ag/oxide/ Sb₂Te₃-Te is estimated to be 1.5×10^{19} /cm³. This is an order of magnitude lower than that of Ag/Sb₂Te₃-Te since the hole density in Ag/Sb₂Te₃-Te (1.6×10^{20} /cm³) is substantially higher than that in Ag/oxide/Sb₂Te₃-Te (5.7×10^{19} /cm³). This suggests that the oxide coating layer is responsible for the overall hole density in a moderate range ($5 - 8 \times 10^{19}$ /cm³). **Figure S1(c)** in the supporting information is the top view of the sample after thermal treatment at 400 °C over one hour. At this extreme temperature, the cast Sb₂Te₃-Te layer mostly sublimed and the particles underneath could be observed. The average size and distribution of the oxide -coated silver NPs were the same as they were before the heating was experimentally initiated (Figure S1 (a)). This result suggests that the oxide-coated silver NPs are inherently thermally stable to 400 °C, which is well above the entire application temperature range from room temperature to 200 °C.

In **Figure 3**, we show the room-temperature Pisarenko plot along with results of theoretical calculation in order to highlight the enhancement of the Seebeck coefficient for Ag/oxide/Sb₂Te₃-Te hetero-structures. Figure 3 and **Table S2** include the results of all the test samples with similar thickness ($\sim 1 \mu\text{m}$). More specifically, the black circles show Sb₂Te₃-Te data; the blue and green circles, data for Ag/oxide/Sb₂Te₃-Te with an optimum oxide thickness (~ 3 nm in total) and the minimum oxide thickness (~ 2 nm in total) respectively; and the orange circles, Ag/Sb₂Te₃-Te without oxide layer. As shown in this plot, Ag/oxide/Sb₂Te₃-Te samples possess moderate hole density in the range $5-8 \times 10^{19}$ /cm³. Moreover, the electronic properties of the samples (green circles) with 2-nm oxide layer (which results in only partial confinement of the silver atoms) are more like those of Ag/Sb₂Te₃-Te with a high carrier density ($> 10^{20}$ /cm³). In order to further compare the Seebeck coefficient enhancement quantitatively, as shown in the inset table, several typical results in Figure 3 were selected and labeled: “Control 1” for Sb₂Te₃-Te, “Control 3” for Ag/Sb₂Te₃, and “Sample” for Ag/oxide/Sb₂Te₃-Te. In addition, a Sb₂Te₃-Te sample with conventional silver doping was prepared by arc melting, followed by the same solution casting route as presented in this paper (“Control 2”). During the synthesis of this control sample, the amount of silver used was chosen on the basis of a previous report^[23] to increase the hole density of Sb₂Te₃-Te slightly to a level equivalent to that of Ag/oxide/Sb₂Te₃-Te. With similar hole densities, 4.0×10^{19} /cm³ for Control 2 and 5.7×10^{19} /cm³ for Sample, the Seebeck coefficient of Ag/oxide/Sb₂Te₃-Te (Sample) is more than 30% higher than that of silver doped Sb₂Te₃-Te (Control 2). We believe this enhancement to be the result of oxide-maintained metal-semiconductor hetero-structures rather than the oxide itself since the oxide itself in this work is barely a dielectric layer with no free carriers, as supported by the evidence in supporting information (Table S1). This enhancement indicates that the efficiency

for this materials system as given by zT was further improved by the hetero-structure design in a manner that has not been reported previously.

In order to better understand this enhancement of S and $S^2\sigma$, simulations were carried out based on various models. To simplify the calculation for $\text{Sb}_2\text{Te}_3\text{-Te}$ (black circles), we assumed a single-phased p-type Sb_2Te_3 with multiple non-parabolic bands, ignoring the existence of excess Te.^[24-26] The calculated Seebeck coefficients for bulk p-type Sb_2Te_3 (light grey curve) steadily decrease with increasing carrier density. Since we applied additional ionized impurity scattering (IIS) to the bulk scattering time to fit the reduced electrical conductivities of the samples, the Seebeck coefficient also shifted up in magnitude by 10~12% at a given carrier density (dark grey curve in Figure 3). The Seebeck coefficients of the control samples that have no silver NPs ($\text{Sb}_2\text{Te}_3\text{-Te}$, black circles) all fall between these two theoretical curves, showing a good agreement with the theory. However, the samples with oxide-coated Ag NPs (Ag/oxide/ $\text{Sb}_2\text{Te}_3\text{-Te}$, blue circles) show much higher Seebeck coefficients than the predicted values by theory at the equivalent carrier densities. Our hypothesis is that this enhancement is due to the carrier energy filtering by the band offset at the interface between the NPs and the matrix. Indeed, theoretical calculations show that this degree of Seebeck enhancement is possible when there is a carrier energy filtering with a cut-off energy ranging from 0.1 to 0.3 eV (color curves) in the material, as shown in Figure 3 and supporting information (**Figure S2** and **Figure S3**).^[27] The cut-off energy is due to the interfacial band offset between the metallic Ag and the semiconducting matrix including both p-type Te and Sb_2Te_3 , and assumes that the dielectric oxide layer is thin enough to not interfere with the band alignment as indicated in **Figure S4**. We propose that this present experimental study is an important evidence for the carrier energy filtering effect occurring in this kind of metal-semiconductor hetero-structures.

It is important to note that the total thickness of the hetero-structure is crucial to the performance as well. The dependence of carrier density and Seebeck coefficient on sample thickness is shown in **Figure S5**. We attribute this dependence to the constant number of activated dopants in telluride after the thin oxide coating, which are concentrated near the bottom of the sample. As the thickness of telluride decreases, total volume decreases but the number of silver dopants remains almost the same, resulting in a higher hole concentration and hence a lower Seebeck coefficient. This behavior of the samples with thicknesses less than 1 μm is similar to what was observed for samples without oxide layers on the silver particles (Ag/ $\text{Sb}_2\text{Te}_3\text{-Te}$), since in both sets of samples, the concentration of silver dopants is high ($> 10^{20} / \text{cm}^3$).

The thermal conductivities were measured by the 3ω method as shown in Figure 4 (a) and described in the supporting information (**Figure S6**).^[28] Compared to the other two control samples, Ag/oxide/ $\text{Sb}_2\text{Te}_3\text{-Te}$ has the lowest thermal conductivity. According to the carrier energy filtering theory,^[27] the Lorenz number is reduced due to inclusion of the transport energy cut-off. We calculate the Lorenz number to be $1.7 \times 10^{-8} \text{ W}\cdot\Omega\cdot\text{K}^{-2}$ for the Ag/oxide/ $\text{Sb}_2\text{Te}_3\text{-Te}$ sample with a 0.2 eV cut-off energy over the temperature range, while the other two samples have the conventional Lorenz number, $L = 2.45 \times 10^{-8} \text{ W}\cdot\Omega\cdot\text{K}^{-2}$, as they are highly degenerate with high doping densities. From the Wiedemann-Franz law, $\kappa_e = L\sigma T$,

we obtain electronic thermal conductivity values of 0.18, 0.37, and 0.22 $\text{W}\cdot\text{m}^{-1}\text{K}^{-1}$ for $\text{Sb}_2\text{Te}_3\text{-Te}$, $\text{Ag/Sb}_2\text{Te}_3\text{-Te}$, and $\text{Ag/oxide/Sb}_2\text{Te}_3\text{-Te}$ samples at room temperature, respectively. The lattice thermal conductivities are 0.84, 1.05, and 0.65 $\text{W}\cdot\text{m}^{-1}\text{K}^{-1}$, for $\text{Sb}_2\text{Te}_3\text{-Te}$, $\text{Ag/Sb}_2\text{Te}_3\text{-Te}$, and $\text{Ag/oxide/Sb}_2\text{Te}_3\text{-Te}$ samples at room temperature, respectively. This indicates that the oxide-coated Ag NPs scatter phonons effectively to reduce the lattice thermal conductivity as shown in Figure 4(a) inset.

In contrast to the typical trend for degenerate semiconductors, the three samples do not show an obvious decrease in thermal conductivity as temperature increases. Note that for $\text{Ag/Sb}_2\text{Te}_3\text{-Te}$, the thermal conductivity increases as temperature increases, consistent with the behavior of metals. This suggests that the silver doping levels of the samples, especially for $\text{Ag/Sb}_2\text{Te}_3\text{-Te}$, are so high that the electronic contribution to the thermal conductivity is significant. This phenomenon has been observed also in the film system previously assembled by nanoparticles.^[19] Using the power factors shown in Figure 2 (d), the estimated zT values are shown in Figure 4(b). The maximum zT for $\text{Ag/oxide/Sb}_2\text{Te}_3\text{-Te}$ is ~ 1.0 at 460 K, more than two times higher than the zT values obtained for the control samples. Note that the zT values are calculated from the in-plane electronic properties (σ and S), and the cross-plane thermal conductivity κ . In this work, according to the calculated in-plane electronic contribution of thermal conductivity (κ_e), the hetero-structure, $\text{Ag/oxide/Sb}_2\text{Te}_3\text{-Te}$, exhibits a lower value for κ_e than the semiconducting reference, $\text{Sb}_2\text{Te}_3\text{-Te}$ (Figure S3), so that as expected, as the dielectric nano-structures are incorporated into the matrix, the overall in-plane lattice thermal conductivity for the heterostructure is estimated to be smaller than the thermal conductivity for the semiconducting matrix, $\text{Sb}_2\text{Te}_3\text{-Te}$. X-ray diffraction patterns are consistent with (see page S-8 in supporting information) the grains of $\text{Sb}_2\text{Te}_3\text{-Te}$ being isotropic, so that one would expect their contribution to the phonon scattering to be similar to the in-plane and cross-plane thermal conductivity of $\text{Sb}_2\text{Te}_3\text{-Te}$. Based on this, the cross-plane thermal conductivity of sample $\text{Sb}_2\text{Te}_3\text{-Te}$ gives an upper limit value of the in-plane thermal conductivity sample $\text{Ag/oxide/Sb}_2\text{Te}_3\text{-Te}$, which is about 10%-20% higher than the measured cross-plane thermal conductivity. This variation is included in the zT values by using the above and the measured cross-plane thermal conductivity to give a possible deviation of 10%-20% in the error bars as shown in Figure 4. The details of this analysis are presented in the supporting information (Figure S7).

In conclusion, a thin oxide layer coating is shown to confine and protect silver NPs, thereby significantly reducing diffusion of silver atoms into the telluride with consequential improved stability of the silver NPs up to 400 °C; while at the same time, the 3-nm oxide layer helps retain the carrier density at $5\times 10^{19}/\text{cm}^3$, resulting in an enhancement of the Seebeck coefficient by $\sim 30\%$ over what was observed for control sample at an equivalent carrier density. This enhancement is accounted for with a simulation that includes an extensive IIS mechanism as well as a cut-off potential of 0.2 eV for hot carrier filtering. The cut-off is the interfacial band offset between the metallic Ag and the semiconducting matrix and we assume that the dielectric oxide coating is thin enough to not interfere with the band alignment, as indicated in Figure S4. The resulting power factor combined with the low thermal conductivity gives a zT of 1.0 at 460 K, significantly higher than reported for materials chemically synthesized previously.^[11,19] To the best of our knowledge, this is the first

successful experimental and theoretical demonstration of a hot carrier filtering effect in a thermally stable metal-semiconductor hetero-structure processed in solution, which opens up a new route for producing TE materials with high efficiencies due to the synergistic increase in both S and σ , with decreasing κ .

Experimental

All reagents were used directly from commercial suppliers without any purification except anhydrous hydrazine. Hydrazine (anhydrous, 98%, Sigma-Aldrich) was distilled firstly and stored in glove box for further use.

Film Preparation:

Step 1: Deposition of 2-dimensional (2D) array of silver NPs. The silver NPs were firstly prepared by e-beam evaporating an 8-nm (mass thickness) silver film (99.999%) on a cleaned quartz substrate then, using rapid thermal annealing to 850 °C for 1 minute, converting the silver film to a 2D array of NPs.

Step 2: Atomic layer deposition (ALD) of dielectric thin layer. Using an atomic layer deposition (ALD) process (Oxford FlexAL), two layers of oxide, aluminum oxide (~1-2 nm) and hafnium oxide (~ 1 nm) were deposited sequentially on the exposed surface of the silver NPs to form the corresponding thin oxide layers. The growth temperatures were 300 °C and 100 °C for aluminum oxide and hafnium oxide respectively. Trimethylaluminum (TMA) and vaporized water, tetrakis(ethylmethylamino) hafnium (TEMAH) and oxygen plasma were the precursors for the growth of Al_2O_3 and HfO_2 respectively. The growth rates and cycles numbers are shown in Table S1.

Step 3: Solution cast of metal chalcogenide. In the final step, the molecular metal chalcogenide (MMC) were prepared following the same procedure previously reported.^[12] The overall concentrations of elemental Te and Sb are about 0.24 M and 0.08 M, respectively. About 5 drops of the as-prepared solution containing Sb and Te were drop-casted to cover the oxide-coated silver nanoparticles. This sample was naturally dried in glove box following annealing at 200 °C for 1 hour under an inert atmosphere. As for the synthesis of sample "Control2" as shown in Figure 3, Ag-doped Sb_2Te_3 and Te was firstly prepared by Arc melting a cold-pressed pellet containing 3.25 g Sb_2Te_3 and 1.8×10^{-3} g Ag powders. The Arc melted product was then grounded into fine powders by regular ball milling and then following the same procedures as other samples for the preparation of the corresponding MMC.

Materials Characterizations

Wide-angle XRD (WAXRD) data were obtained on a Philips X'Pert with Cu $K\alpha$ radiation and Rietveld-refined using ReX software (<http://www.rexpd.com/rex/>). The powder patterns of all crystalline phases were refined using fits with lattice cell parameters of Sb_2Te_3 (JCPDS 015-0874) and Te (JCPDS 089-4899). Scanning electron microscopy (SEM) images were taken on a Philips XL40 electron microscope after low angle ion milling in the FEI DB235 dual-beam FIB system. A Physical Electronics 6650 Dynamic Secondary Ion Mass Spectrometry (SIMS) system was used to measure the ^{107}Ag to ^{128}Te ratio. A Dektak VI Profilometer tested the average thickness of each sample.

Measurements of Electronic Properties: 150-nm-thick Au contacts were thermally deposited on the film following van der Pauw pattern. A detailed description of the Hall and Seebeck measurements can be found in the literature.^[12]

Measurements of Thermal Conductivities: For the thermal conductivity measurement, the film was deposited on a Si wafer with ~ 200 nm thermally grown oxide instead of using quartz. The plasma enhanced chemical vapor deposition (PECVD) was applied to grow a silica layer (~ 500 nm) on top of the film. A wire made of 4000 \AA of Au on top of 200 \AA of Ti, which functioned as both heater and thermometer, was patterned on each sample surface and fabricated by photolithography, e-beam evaporation, and finally lift-off. These processing procedures were kept consistent in the preparation of both bare reference without telluride film and the real sample. The electrical resistance and the coefficient dR/dT of the metal wire were determined by measuring the electrical resistance at different temperatures between 20 and 200 °C. The third-harmonic voltage drop across the metal wire was measured at five different frequencies between 500 and 2 kHz.

Simulations: We modeled the carrier transport in bulk Sb_2Te_3 based on the Boltzmann transport under the relaxation time approximation.^[24] Multiple non-parabolic bands were considered in the model with anisotropic effective masses. Antimony telluride has a rhombohedral crystal structure with a small direct band gap of ~ 100 meV at the center of the Brillouin zone (BZ), Γ valley.^[25] Two other valence bands on the lines Γ -U and Z-F in the BZ have their band maxima close to that of the primary valence band.^[25,26] The acoustic phonon deformation potential scattering, polar optical phonon scattering, and the screened ionized impurity scattering were included in the bulk transport model. The charge carrier energy filtering scheme was then applied to the bulk model by introducing a cut-off energy level E_C in the transport integrals. It is assumed in the calculations that below the cut-off energy, all the carriers are prevented from participating in the conduction. Details of the carrier energy filtering theory are described elsewhere.^[27]

Acknowledgments

Y.Z. and J.H.B. sincerely thank A. Gossard and P. Burke for helpful discussions and A. Szein, P. Burke, B. Curin, and H. Lu for assistance with instrument use. This work was primarily supported as part of the Center for Energy Efficient Materials, an Energy Frontier Research Center funded by the U.S. Department of Energy, Office of Science, Basic Energy Sciences under Award # DE-SC0001009. The characterizations used the MRL Central Facilities, supported by the MRSEC Program of the NSF under Award No. DMR 1121053; a member of the NSF-funded Materials Research Facilities Network (www.mrfn.org). C.S.B. acknowledges the Feodor Lynen Research Fellowship supported by the Alexander von Humboldt Foundation.

(Supporting Information is available online from Wiley InterScience or from the author).

- [1] Y. Zhang, H. Wang, S. Kraemer, Y. Shi, F. Zhang, M. L. Snedaker, K. Ding, M. Moskovits, G. J. Snyder, G. D. Stucky, *ACS Nano* **2011**, *5*, 3158–3165.
- [2] G. Joshi, X. Yan, H. Wang, W. Liu, G. Chen, Z. Ren, *Adv. Energy Mater.* **2011**, *1*, 643–647.
- [3] B. Poudel, Q. Hao, Y. Ma, Y. Lan, A. Minnich, B. Yu, X. Yan, D. Wang, A. Muto, D. Vashaee, X. Chen, J. Liu, M. S. Dresselhaus, G. Chen, Z. Ren, *Science* **2008**, *320*, 634–638.
- [4] G. Joshi, B. Poudel, Q. Hao, Y. Ma, Y. Lan, A. Minnich, B. Yu, X. Yan, D. Wang, A. Muto, D. Vashaee, X. Chen, J. Liu, M. S. Dresselhaus, G. Chen, Z. Ren, *Nano Lett.* **2008**, *8*, 4670–4674.
- [5] J. Tang, H. Wang, D. H. Lee, M. Fardy, Z. Huo, T. P. Russell, P. Yang, *Nano Lett.* **2010**, *10*, 4279–4283.
- [6] Y. Zhang, T. Day, M. L. Snedaker, H. Wang, S. Krämer, C. S. Birkel, X. Ji, D. Liu, G. J. Snyder, G. D. Stucky, *Adv. Mater.* **2012**, *24*, 5065–5670.
- [7] G. J. Snyder, E. S. Toberer, *Nat. Mater.* **2008**, *7*, 105–514.
- [8] K. Biswas, J. He, I. D. Blum, C. Wu, T. P. Hogan, D. N. Seidman, V. P. Dravid, M. G. Kanatzidis, *Nature* **2012**, *489*, 414–418.
- [9] D. G. Cahill, S. K. Watson, R. O. Pohl, *Phys. Rev. B* **1992**, *46*, 6131–6140.
- [10] J. P. Heremans, V. Jovovic, E. S. Toberer, A. Saramat, K. Kurosaki, A. Charoenphakdee, S. Yamanaka, G. J. Snyder, *Science* **2008**, *321*, 554–557.
- [11] D.-K. Ko, Y. Kang, C. B. Murray, *Nano Lett.* **2011**, *11*, 2841–2844.
- [12] Y. Zhang, M. L. Snedaker, C. S. Birkel, S. Mubeen, X. Ji, Y. Shi, D. Liu, X. Liu, M. Moskovits, G. D. Stucky, *Nano Lett.* **2012**, *12*, 1075–1080.
- [13] W. Kim, S. L. Singer, A. Majumdar, D. Vashaee, Z. Bian, A. Shakouri, G. Zeng, J. E. Bowers, J. M. O. Zide, A. C. Gossard, *Appl. Phys. Lett.* **2006**, *88*, 242107.
- [14] K. F. Hsu, S. Loo, F. Guo, W. Chen, J. S. Dyck, C. Uher, T. Hogan, E. K. Polychroniadis, M. G. Kanatzidis, *Science* **2004**, *303*, 818–821.
- [15] Y. Liu, P. Sahoo, J. P. A. Makongo, X. Zhou, S.-J. Kim, H. Chi, C. Uher, X. Pan, P. F. P. Poudeu, *J. Am. Chem. Soc.* **2013**, *135*, 7486–7495.
- [16] M. G. Kanatzidis, *Chem. Mater.* **2010**, *22*, 648–659.
- [17] M. Scheele, N. Oeschler, I. Veremchuk, S.-O. Peters, A. Littig, A. Kornowski, C. Klinke, H. Weller, *ACS Nano* **2011**, *5*, 8541–8551.
- [18] R. Y. Wang, J. P. Feser, X. Gu, K. M. Yu, R. A. Segalman, A. Majumdar, D. J. Milliron, J. J. Urban, *Chem. Mater.* **2010**, *22*, 1943–1945.
- [19] M. V. Kovalenko, B. Spokoyny, J.-S. Lee, M. Scheele, A. Weber, S. Perera, D. Landry, D. V. Talapin, *J. Am. Chem. Soc.* **2009**, *131*, 597–602.
- [20] D. B. Mitzi, L. L. Kosbar, C. E. Murray, M. Copel, A. Afzali, *Nature* **2004**, *428*, 299–303.
- [21] S. Faleev, F. Léonard, *Phys. Rev. B* **2008**, *77*, 214304.
- [22] A. Popescu, L. Woods, J. Martin, G. Nolas, *Phys. Rev. B* **2009**, *79*, 205302.
- [23] J. Horlk, M. Stordeur, *Phys. Status Solidi B* **1982**, *114*, 39–45.
- [24] J.-H. Bahk, Z. Bian, M. Zebarjadi, J. M. O. Zide, H. Lu, D. Xu, J. P. Feser, G. Zeng, A. Majumdar, A. C. Gossard, A. Shakouri, J. E. Bowers, *Phys. Rev. B* **2010**, *81*, 235209.
- [25] B. Y. Yavorsky, N. F. Hinsche, I. Merting, P. Zahn, *Phys. Rev. B* **2011**, *84*, 165208.
- [26] T. Thonhauser, T. J. Scheidemann, J. O. Sofo, J. V. Badding, G. D. Mahan, *Phys. Rev. B* **2003**, *68*, 085201.

- [27] J.-H. Bahk, Z. Bian, A. Shakouri, *Phys. Rev. B* **2013**, *87*, 075204.
- [28] D. G. Cahill, *Rev. Sci. Instrum.* **1990**, *61*, 802–808.

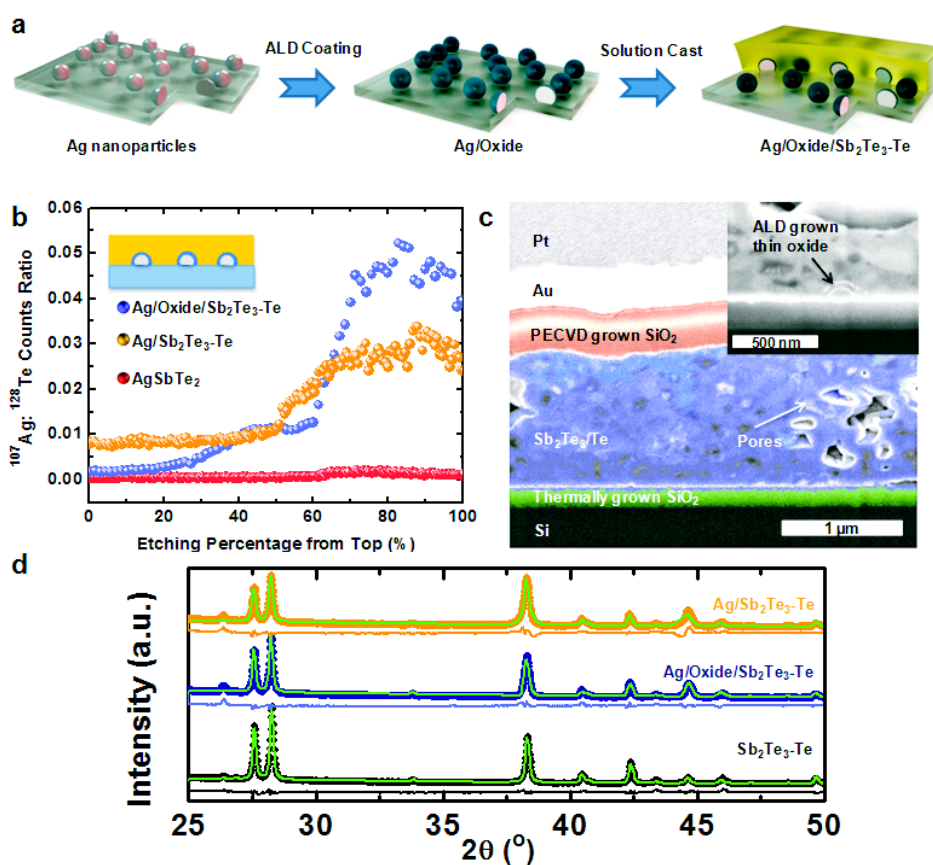


Figure 1. (a) Schematic depiction of the synthesis procedures. (b) The SIMS signal ratio between ^{107}Ag and ^{128}Te in three samples: AgSbTe₂, Ag/Sb₂Te₃-Te and Ag/oxide/Sb₂Te₃-Te. The inset is the schematic structure of Ag/oxide/Sb₂Te₃-Te. (c) Cross-sectional SEM image of Ag/oxide/Sb₂Te₃-Te; the inset corresponds to the zoom-in image on the interface between Sb₂Te₃-Te (blue layer) and substrate (green layer). (d) X-ray diffraction patterns of Sb₂Te₃-Te (black), Ag/oxide/Sb₂Te₃-Te (blue) and Ag/Sb₂Te₃-Te (orange). The green patterns are the calculated pattern after Rietveld refinement, the curve under each pattern corresponds to the error.

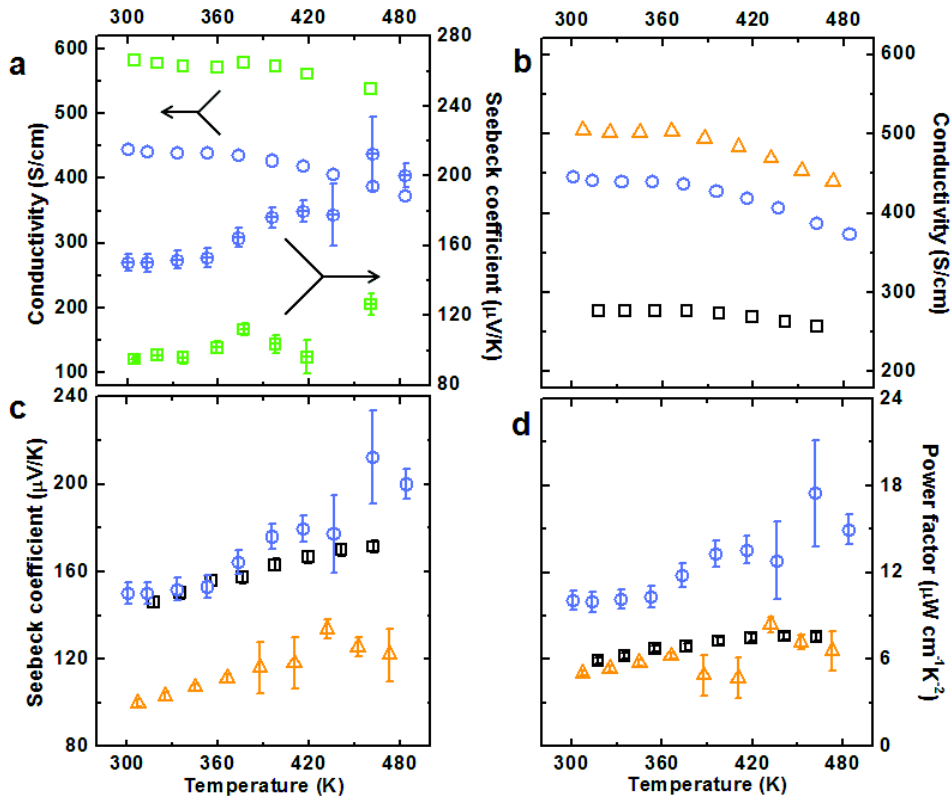


Figure 2. (a) The temperature dependence of electrical conductivities and Seebeck coefficients of Ag/oxide/Sb₂Te₃-Te samples with 2-nm oxide layer in total (green squares \square) and 3-nm oxide layer in total (blue circles \circ); (b)-(d) The temperature dependence of electrical conductivities (b), Seebeck coefficients (c) and power factors (d) of sample Sb₂Te₃-Te (black squares \square), Ag/oxide/Sb₂Te₃-Te (blue circles \circ) and Ag/Sb₂Te₃-Te (orange triangles \triangle). The error bars of Seebeck coefficients in (a) and (c) include the variation from batch to batch and the measurement error from cycle to cycle. Compared to the Seebeck coefficient errors, the test errors in the measurement of the electrical conductivities (b) are negligible. In addition, no significant trend of variation can be observed from the first cycle to the last.

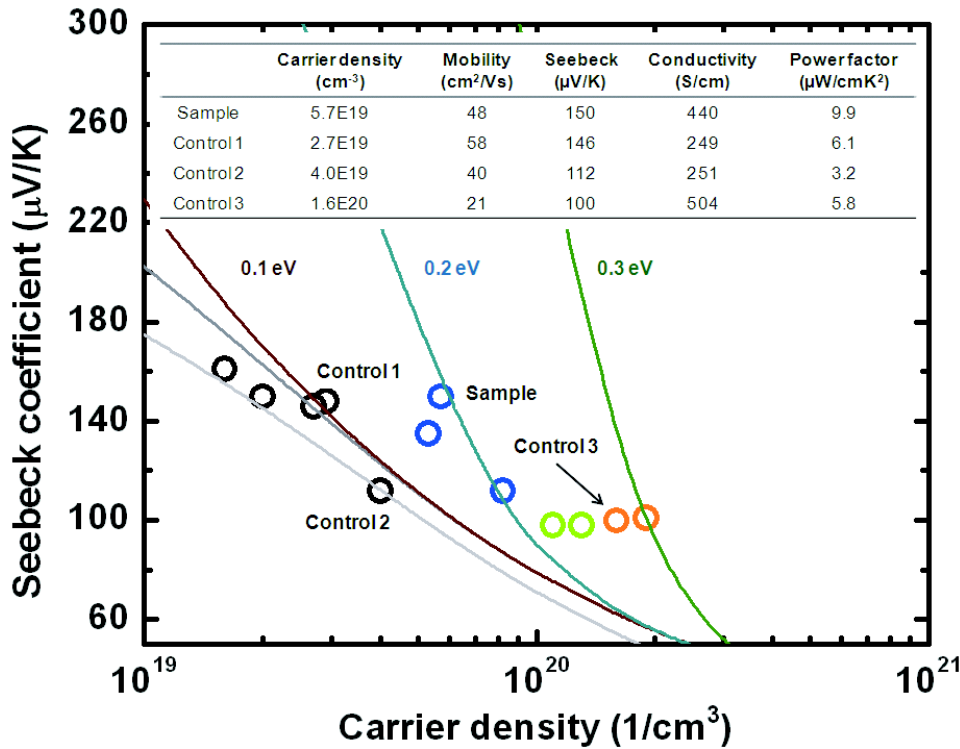


Figure 3. Seebeck coefficients as a function of carrier densities at room temperature. The error bars correspond to the measurement errors. The black circles represent the set of $\text{Sb}_2\text{Te}_3\text{-Te}$ with no Ag and no oxide (“Control 1” is selected from this group), and $\text{Sb}_2\text{Te}_3\text{-Te}$ with conventional Ag doping by arc-melting (“Control 2” selected); blue circles represent Ag/oxide/ $\text{Sb}_2\text{Te}_3\text{-Te}$ with 3-nm oxide layer in total (“Sample” selected); green ones represent Ag/oxide/ $\text{Sb}_2\text{Te}_3\text{-Te}$ with 2-nm oxide layer in total, and the orange circles represent the set of Ag/ $\text{Sb}_2\text{Te}_3\text{-Te}$ with no oxide (“Control 3” selected). The light grey curve represents the calculated Seebeck coefficient based on bare Sb_2Te_3 semiconducting band without adding the ionized scattering strength; the dark grey curve adds the effect of additional ionized scattering strength to fit the experimental electrical conductivity; and the color curves are the calculated Seebeck coefficients based on the hot carrier filtering effect in Sb_2Te_3 with a cut-off band potential of 0.1 eV (dark red), 0.2 eV (dark cyan) and 0.3 eV (dark green) respectively. The inset is the table of the electronic properties of the selected Sample and Controls.

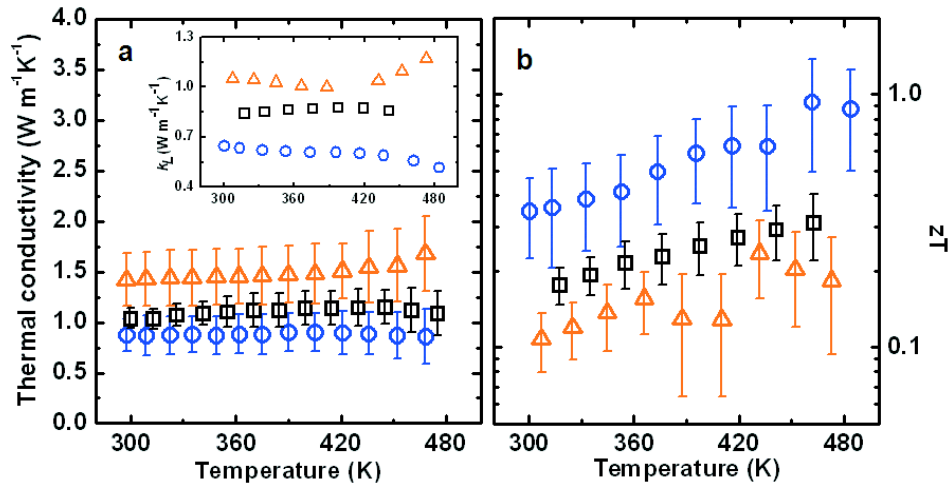


Figure 4. The temperature dependence of thermal conductivities (a), lattice thermal conductivities (the inset in a) and zT s (b) of sample Sb₂Te₃-Te (black squares \square), Ag/oxide/Sb₂Te₃-Te (blue circles \circ), and Ag/Sb₂Te₃-Te (orange triangles \triangle). The standard deviations in the observed thermal conductivity values of all the samples are mainly due to the surface roughness of the samples.

This work describes an approach based on a solution-based synthesis that produces a thermally stable Ag/oxide/Sb₂Te₃-Te metal-semiconductor hetero-structure that achieves a figure of merit $zT = 1.0$ at 460 K, a record for a hetero-structured material made by using wet chemistry. Combining experiments and theory shows that the large increase in the material's Seebeck coefficient results from hot carrier filtering.

Keyword thermoelectric, hot carrier filtering effect, solution processed, hetero-structure, molecular metal chalcogenide, atomic layer deposition (ALD)

Yichi Zhang, Je-Hyeong Bahk, Joun Lee, Christina S. Birkel, Matthew L. Snedaker, Deyu Liu, Hongmei Zeng, Martin Moskovits, Ali Shakouri, and Galen D. Stucky*

Title (Hot Carrier Filtering in Solution Processed Hetero-structures: a Paradigm for Improving Thermoelectric Efficiency)

ToC figure

